Letter

Mirror symmetry protected higher-order topological zero-frequency boundary and corner modes in Maxwell lattices

Siddhartha Sarkar,* Xiaoming Mao,† and Kai Sun‡
Department of Physics, University of Michigan, Ann Arbor, Michigan 48109, USA

(Received 20 April 2023; revised 28 July 2023; accepted 3 August 2023; published 15 August 2023)

Maxwell lattices, where the number of degrees of freedom equals the number of constraints, are known to host topologically protected zero-frequency modes and states of self-stress, characterized by a topological index called topological polarization. In this Letter, we show that in addition to these known topological modes, with the help of a mirror symmetry, the inherent chiral symmetry of Maxwell lattices creates another topological index, the mirror-graded winding number (MGWN). This MGWN is a higher-order topological index, which gives rise to topological zero modes and states of self-stress at mirror-invariant domain walls and corners between two systems with different MGWNs. We further show that two systems with the same topological polarization can have different MGWNs, indicating that these two topological indices are fundamentally distinct.

DOI: 10.1103/PhysRevB.108.L060103

Introduction. Bulk-boundary correspondence is a defining feature of topological states where the nontrivial topology of the bulk gives rise to modes localized at the boundary [1,2]. Early research on topological band theory focused on d-dimensional topological systems with localized states at $(d-1)$-dimensional boundaries (e.g., the quantum Hall effect [3], quantum anomalous Hall effect [4], and quantum spin Hall effect [5,6]); this type of topology is now called first-order topology. A new kind of topological states, called higher-order topological states (HOTS), has been proposed in the last five years [7–9]. Here, instead of having $(d-1)$-dimensional topologically protected boundary modes, the d-dimensional nth-order topological system has $(d-n)$-dimensional $(n>1)$ boundary modes. The boundary modes corresponding to $n=d$ and $n=d-1$ are generally called corner and hinge modes, respectively. These higher-order states are generally protected by crystalline symmetries such as mirror [10], inversion [11], rotation [12,13], product of time reversal (TRS) and rotation [9], etc. (see Ref. [14] for an exhaustive literature survey). Along with realizations in electronic systems, crystalline symmetry protected HOTS have been implemented in mechanical/elastic systems too, offering a class of materials in which elastic energy can be selectively confined to low-dimensional regions [15–20].

One key challenge in the study of HOTS lies in the stability of topological corner modes. For example, in contrast to the quantum Hall effect, where the topological edge modes remain stable for *any* boundary conditions, for a two-dimensional (2D) HOTS, unless a certain special ingredient is introduced (e.g., a chiral symmetry), the frequency of the topological corner modes is in general not pinned to a particular value. Thus, depending on the microscopic details, such as boundary conditions and disorder near the corners, these topological modes can disappear into bulk bands [21,22]. To overcome this challenge, recently, a generalized chiral symmetry was introduced to realize corner modes in a breathing kagome lattice acoustic metamaterial [20], while there are still some open discussions about the topological origin of these modes [22,23]. Another attempt [24] showed the existence of corner modes pinned at zero frequency in an overconstrained system made of rigid quadrilaterals connected by free hinges, however, this can be understood within the framework of boundary obstructed topological phases [25].

In this Letter, we provide a different approach towards HOTS using Maxwell lattices [i.e., lattices with equal numbers of degrees of freedom (DOF) n_d and constraints n_c [26,27]], and show that the intrinsic chiral symmetry protected by this counting extends robustness to topological corner modes in these lattices, without requiring any detailed matching at the boundaries. As shown by Kane and Lubensky [28], Maxwell systems can be mapped to a superconducting Bogoliubov–de Gennes (BdG) Hamiltonian, which naturally has a chiral symmetry. With the BdG Hamiltonian, a first-order topological index, the topological polarization, can be introduced [28], resulting in topologically protected edge modes at zero frequency. We find that in addition to this first-order topological index, a nontrivial higher-order topological index [the mirror-graded winding number (MGWN) [29–31]] can be introduced to Maxwell lattices, controlling zero-frequency topological domain-wall/corner modes, with robustness originating from the intrinsic chiral symmetry of the locking of degrees of freedom and constraints in Maxwell lattices.

Kane-Lubensky topological index of Maxwell lattices. The linear mechanics of lattices made of point masses connected by springs is characterized by the compatibility matrix $\mathbf{C}$ which relates extensions of springs $e_i = C_{ij}u_j$ to the displacements u_i of the point masses. Furthermore, $f_i = C_{ij}^T t_j$ relates the forces f_i on the point masses to the tensions t_i in the

*sarkarsi@umich.edu
†maox@umich.edu
‡sunkai@umich.edu

springs. In Fourier space, the matrix $\mathbf{C}(\mathbf{q})$ has the size $n_c \times n_d$. The normal mode frequencies of these lattices $\omega^2(\mathbf{q})$ are the eigenvalues of the dynamical matrix $\mathbf{D}(\mathbf{q}) = \mathbf{C}^\dagger(\mathbf{q})\mathbf{C}(\mathbf{q})$. Kane and Lubensky [28] defined a "square root" of the dynamical matrix, which in reciprocal space takes the following form:

$$\mathcal{H}(\mathbf{q}) = \begin{pmatrix} \mathbf{0} & \mathbf{C}^\dagger(\mathbf{q}) \\ \mathbf{C}(\mathbf{q}) & \mathbf{0} \end{pmatrix}. \tag{1}$$

For every nonzero eigenvalue $\omega^2(\mathbf{q})$ of $\mathbf{D}(\mathbf{q})$, $\mathcal{H}(\mathbf{q})$ has two eigenvalues $\pm\omega(\mathbf{q})$. The zero modes of $\mathcal{H}(\mathbf{q})$ include nullspace of $\mathbf{C}(\mathbf{q})$ [zero modes (ZMs)] and nullspace of $\mathbf{C}^\dagger(\mathbf{q})$ [states of self-stress (SSS)], whereas the zero modes of $D(\mathbf{q})$ include the ZMs. The Maxwell-Calladine theorem [26,32] dictates that the number of ZMs (n_0) and number of SSS (n_s) are equal ($n_0 = n_s$) for a Maxwell lattice. The matrix $\mathcal{H}(\mathbf{q})$ has the property that $S\mathcal{H}(\mathbf{q})S = -\mathcal{H}(\mathbf{q})$, where $S = \mathrm{Diag}\{\mathbb{1}, -\mathbb{1}\}$. This property is known as the chiral (or sublattice) (anti)symmetry in the literature. Also, it is easy to check that $\mathcal{H}(\mathbf{q})$ has TRS, $\mathcal{H}(\mathbf{q}) = \mathcal{H}^*(-\mathbf{q})$, where * is complex conjugation. These two symmetries put the matrix $\mathcal{H}(\mathbf{q})$ in the BDI class of Altland-Zirnbauer classification [33–36]. Along a closed loop l in the Brillouin zone where the spectrum of the matrix is gapped at zero, a topological invariant n_l can be defined, $n_l = \frac{1}{2\pi i}\oint_l d\mathbf{q}\cdot\nabla_{\mathbf{q}} \log\det \mathbf{C}^\dagger(\mathbf{q})$, which controls the number of topological ZMs at an open edge or domain walls.

Mirror-graded winding number. Interestingly, in mirror symmetric Maxwell lattices, along the mirror-invariant lines in the Brillouin zone, the mirror reflection operator $\mathbf{M}(\mathbf{q})$ commutes with the matrix $\mathcal{H}(\mathbf{q})$. Consequently, $\mathbf{M}(\mathbf{q})$ and $\mathcal{H}(\mathbf{q})$ can be simultaneously diagonalized. Since, $\mathbf{M}(\mathbf{q})$ only takes eigenvalues ± 1, using the eigenvectors of $\mathbf{M}(\mathbf{q})$ the matrices $\mathbf{C}(\mathbf{q})$ and $\mathcal{H}(\mathbf{q})$ can be block-diagonalized into odd ($-$) and even ($+$) sectors [Supplemental Material (SM) [37] Secs. SM2 and SM3]:

$$\mathbf{C}(\mathbf{q}) = \begin{pmatrix} \mathbf{C}_-(\mathbf{q}) & \mathbf{0} \\ \mathbf{0} & \mathbf{C}_+(\mathbf{q}) \end{pmatrix}, \tag{2a}$$

$$\mathcal{H}(\mathbf{q}) = \begin{pmatrix} \mathbf{0} & \mathbf{C}_-^\dagger(\mathbf{q}) & \mathbf{0} & \mathbf{0} \\ \mathbf{C}_-(\mathbf{q}) & \mathbf{0} & \mathbf{0} & \mathbf{0} \\ \mathbf{0} & \mathbf{0} & \mathbf{0} & \mathbf{C}_+^\dagger(\mathbf{q}) \\ \mathbf{0} & \mathbf{0} & \mathbf{C}_+(\mathbf{q}) & \mathbf{0} \end{pmatrix}. \tag{2b}$$

Now, using $\mathbf{C}_\pm(\mathbf{q})$ we can define a topological invariant in each sector, the MGWNs,

$$\nu_\pm = \frac{1}{2\pi i}\oint_{\mathbf{q}\to\mathbf{q}+\mathbf{G}_m} d\mathbf{q}\cdot\nabla_{\mathbf{q}} \log\det \mathbf{C}_\pm^\dagger(\mathbf{q}), \tag{3}$$

where $\mathbf{G}_m$ is the smallest reciprocal lattice vector along the mirror plane [29–31]. Note that $\nu_+ + \nu_- = n_l$, since in this basis $\det\mathbf{C}(\mathbf{q}) = \det\mathbf{C}_+(\mathbf{q})\det\mathbf{C}_-(\mathbf{q})$. In other words, the mirror symmetry allows us to split topological polarization into two different topological indices ν_+ and ν_-. This observation expanded the topological classification of Maxwell lattices, and allows us to realize HOTS.

It is worthwhile to highlight that to define a topological index, the Hamiltonian [Eq. (2)] must remain gapped with $\det\mathbf{C} \neq 0$. Because a mirror plane in the momentum space often passes through the Γ point ($k = 0$), it is necessary to gap the acoustic phonon bands at Γ. As will be shown below, this can be achieved by restricting the motion of certain lattice points, which break the translational invariance of the lattice.

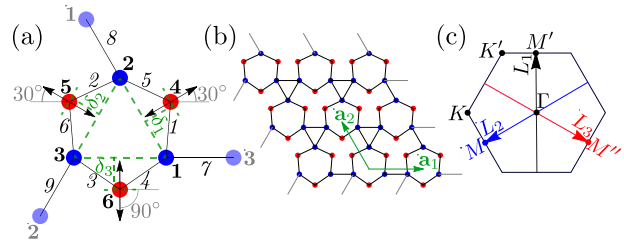

FIG. 1. The mirror symmetric Maxwell lattice. (a) The unit cell consists of three blue and three red point masses enumerated by bold numbers. The blue points can move in both the x and y directions whereas the red points can only move along the direction of the corresponding double-directional black arrow. Parameter δ_i ($i = 1, \ldots, 3$) is the perpendicular distance of point $i+3$ from the line joining points i and $i+1$. The numbers in italics enumerate the springs. The partially transparent blue points are in adjacent unit cells. (b) A 3×3 lattice. The springs shown in gray at the edges are required for a periodic boundary condition. The green arrows show the lattice vectors. (c) First Brillouin zone with the high-symmetry points. The noncontractible loop L_i is invariant under mirror reflection when $\delta_i = \delta_{i+1}$.

The mirror symmetric Maxwell lattice. We now illustrate one Maxwell lattice that supports HOTS. As shown in Fig. 1, each unit cell of this lattice contains six point masses with coordinates

$$\mathbf{r}_i = \frac{1}{3}\left[\cos\left(\frac{2\pi i}{3} - \frac{5\pi}{6}\right), \sin\left(\frac{2\pi i}{3} - \frac{5\pi}{6}\right)\right], \tag{4a}$$

$$\mathbf{r}_{i+3} = \left(\frac{1}{6} + \delta_i\right)\left[\cos\left(\frac{2\pi i}{3} - \frac{\pi}{2}\right), \sin\left(\frac{2\pi i}{3} - \frac{\pi}{2}\right)\right], \tag{4b}$$

with $i \in \{1, 2, 3\}$. The three points $i = 1$, 2, and 3 can move in both x and y directions, while the other three are restricted to move along the direction marked by the black arrows shown in Fig. 1(a),

$$\mathbf{u}_i = (u_{ix}, u_{iy}), \tag{5a}$$

$$\mathbf{u}_{i+3} = u_{i+3}\left[\cos\left(\frac{2\pi i}{3} - \frac{\pi}{2}\right), \sin\left(\frac{2\pi i}{3} - \frac{\pi}{2}\right)\right], \tag{5b}$$

for $i \in \{1, 2, 3\}$. Consequently, there are $n_d = 9$ DOF per unit cell $\{u_{1x}, u_{1y}, \ldots, u_{3y}, u_4, u_5, u_6\}$.

We then repeat this unit cell to form a 2D lattice and connect the mass points with springs [solid lines in Fig. 1(b)]. Here, we set the lattice vectors $\mathbf{a}_1 = (1, 0)$ and $\mathbf{a}_2 = \frac{1}{2}(-1, \sqrt{3})$, and the masses of all points and the stiffnesses of all springs are set to 1 for simplicity. Notice that here we have nine springs per unit cell, which match the DOFs $n_d = 9$, making the system a Maxwell lattice.

Note that if we set $\delta_i = \delta_{i+1}$, the system is invariant under mirror reflection about the perpendicular bisector of points $i+3$ and $i+4$. The corresponding mirror-invariant lines L_i in the reciprocal space (Brillouin zone) are shown in Fig. 1(c). Because all the mirror planes go through Γ, it is important to gap out the phonon bands at Γ to define the topological index. In this setup, this is automatically achieved because points

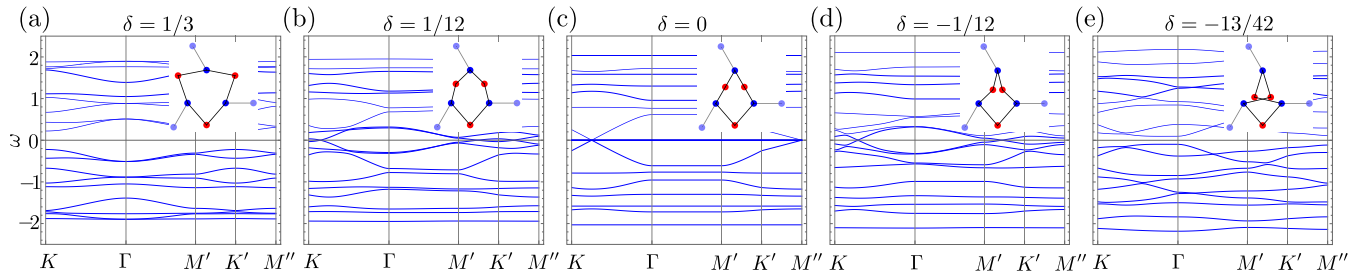

FIG. 2. Spectrum of $\mathcal{H}$ for different values $\delta = \delta_1 = \delta_2$ keeping $\delta_3 = 1/3$. The unit cell corresponding to each configuration is shown in the inset. Each diagram has $n_c + n_d = 18$ bands. All systems except (c) are gapped along the line Γ-M' [L_1 in Fig. 1(c)]. (c) has four flat bands at zero frequency. The spectra in (b) and (d) are gapped at $\omega = 0$ along the line Γ-M', but not gapped everywhere in the Brillouin zone. Only (a) and (e) are fully gapped at $\omega = 0$ over the entire Brillouin zone.

$i = 4, 5, 6$ can only move along the arrow directions, which gaps out the acoustic modes.

The compatibility matrix $\mathbf{C}(\mathbf{q})$ is given in SM [37] Sec. SM1. For simplicity we set $\delta_3 = 1/3$ and vary $\delta_1 = \delta_2 \equiv \delta$. In this case, the lattice has one mirror m_x per unit cell normal in the x direction. Along the mirror-invariant line $q_x = 0$ [L_1 in Fig. 1(c)], we calculate $\det \mathbf{C}_+^\dagger|_{L_1}$, $\det \mathbf{C}_-^\dagger|_{L_1}$ and integrate them from $\mathbf{q} = (0, -2\pi/\sqrt{3})$ to $\mathbf{q} + \mathbf{b}_2 = (0, 2\pi/\sqrt{3})$ along path L_1 according to Eq. (3). We find

$$\nu_+ = \begin{cases} 1 & \text{if } \delta > 0, \\ 0 & \text{if } \delta < 0, \end{cases} \quad \nu_- = \begin{cases} 0 & \text{if } \delta > 0, \\ 1 & \text{if } -5/12 < \delta < 0, \\ 0 & \text{if } \delta < -5/12. \end{cases} \tag{6}$$

Clearly, the phases with $\delta > 0$ and $0 > \delta > -5/12$ are distinct with respect to the MGWNs but the same with respect to the Kane-Lubensky index. We will call $\delta > 0$ phase 1, and $0 > \delta > -5/12$ phase 2. In Fig. 2, we show the spectrum of matrix $\mathcal{H}(\mathbf{q})$ for different values of δ. At $\delta = 0$, the DOF corresponding to points **4** and **5** are perpendicular to the springs connected to them, hence displacements of these points do not change the length of the springs to the linear order. These give two ZMs at every wave vector $\mathbf{q}$. Then, due to the Maxwell-Calladine index theorem there are two SSS at every $\mathbf{q}$. Hence, there are four flat bands at $\omega = 0$ of the matrix $\mathcal{H}(\mathbf{q})$ for $\delta = 0$. When $\delta \neq 0$, $\omega = 0$ gapped along the C_1 line, allowing us to define the MGWNs $\nu_\pm$.

In addition to defining the MGWNs, in order to localize ZMs at the junction of two different mirror-graded phases, we require the bulk bands to be completely gapped at $\omega = 0$ in addition to the path L_1. We find that phase 1 is fully gapped at $\omega = 0$ over the entire Brillouin zone for $\delta > 5/42$ [Fig. 2(a)], whereas phase 2 is fully gapped for $-5/12 < \delta < -1/6$ [Fig. 2(e)] (see SM [37] Sec. SM4 for details).

Mirror-protected zero-frequency edge states. To examine the bulk-edge correspondence, we create a supercell in Fig. 3 with periodic boundary conditions in both directions, which has domain walls separating $\delta = 1/3$ and $\delta = -13/42$. The domain walls are horizontal—normal to the mirror m_x, hence invariant under reflection about the mirror m_x. The spectrum of the dynamical matrix $\mathbf{D}(q_x)$ of the system is plotted as a function of surface wave vector q_x. We find two ZMs at $q_x = 0$ [Fig. 3(a)]. Since the Kane-Lubensky indices of both domains are the same, $n^{\delta=1/3} = \nu_+^{\delta=1/3} + \nu_-^{\delta=1/3} = 1 = \nu_+^{\delta=-13/42} + \nu_-^{\delta=-13/42} = n^{\delta=-13/42}$, the ZMs at the domain walls are not given by the Kane-Lubensky index. However, since at $q_x = 0$, matrix $\mathbf{C}(\mathbf{q})$ can be block-diagonalized [Eq. (2)] as discussed above, we can use Eq. (3) on the + and − sectors separately. Since matrix $\mathbf{C}(q_x = 0, q_y)$ is block-diagonal, the ZMs of each sector are also ZMs of the full system. Hence, at the top and bottom domain walls we get

$$\text{top wall:} \quad \nu_+^< - \nu_+^> = 1 \Rightarrow \text{ZM}, \quad \nu_-^< - \nu_-^> = -1 \Rightarrow \text{SSS}, \tag{7a}$$

$$\text{bottom wall:} \quad \nu_+^< - \nu_+^> = -1 \Rightarrow \text{SSS}, \quad \nu_-^< - \nu_-^> = 1 \Rightarrow \text{ZM}, \tag{7b}$$

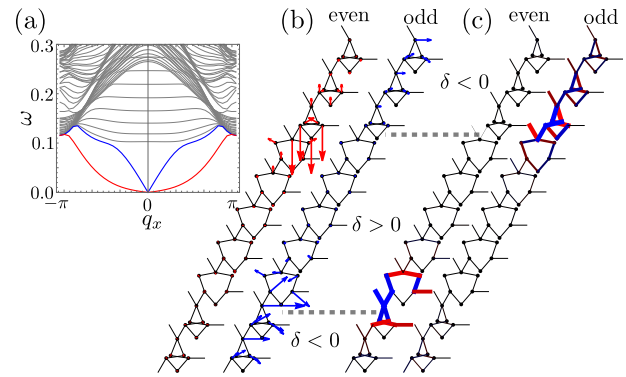

FIG. 3. (a) Spectrum, (b) ZMs, and (c) SSS of a supercell consisting of $2N_0$ unit cells among which N_0 in the middle have $\delta = 1/3$ and the other ones have $\delta = -13/42$. A periodic boundary condition is employed in the direction $(1/2, \sqrt{3}/2)$, whereas a Bloch-periodic boundary condition $\mathbf{u}[\mathbf{x} + (1, 0)] = \mathbf{u}(\mathbf{x})e^{iq_x}$ is employed in the (1,0) direction. In (a), gray bands are bulk modes whereas the red and the blue bands are localized at the top and bottom domain walls, respectively. The left ZM in (b) is localized at the top domain wall and is even under vertical mirror m_x, whereas the right ZM in (b) is localized at the bottom domain wall and is odd under vertical mirror m_x. The left SSS in (c) is localized at the bottom domain wall and is even under vertical mirror m_x, whereas the right SSS in (c) is localized at the top domain wall and is odd under vertical mirror m_x. The red and blue colors of the bonds in (c) indicate the elongation and compression of the bonds, respectively.

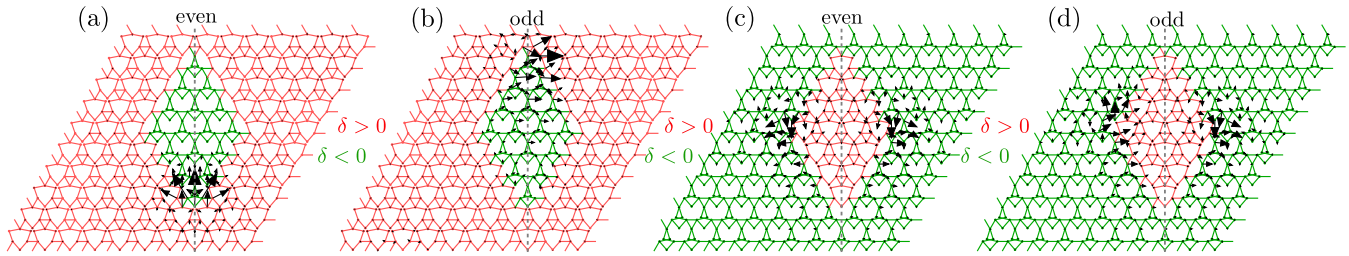

FIG. 4. Corner modes in systems with a diamond-shaped island of one phase inside another phase. In each panel, the part of the system in red (green) has $\delta = 1/3$ ($\delta = -13/42$). The vertical gray dashed lines show the line of mirror symmetry; it passes through the top and bottom corners of the diamond-shaped island. We applied periodic boundary conditions in all cases. The black arrows show the displacement field corresponding to the zero modes. In all cases, the zero modes are concentrated at the corners. The corner modes in (a) and (c) are even under the vertical mirror reflection, whereas (b) and (d) are odd under the same reflection.

where $<$ and $>$ denote phases below and above the domain wall, respectively. It must be emphasized here that because rigid translation is not a zero mode in our lattice, in general such a lattice is not expected to have zero modes and all phonon modes should be gapped. However, at the domain boundary between regions with different topological indices, topological edge modes emerge with frequency pinned to zero by the chiral symmetry.

It is also worthwhile to highlight that these topological zero modes are fundamentally different from the zero modes protected by topological polarization. First, they are due to a totally different topological index. Second, in contrast to zero modes from topological polarization, the supercell spectrum of which has flat bands at zero frequency [28], the topological modes here are dispersive. Because the mirror symmetry is broken away from the mirror plane ($q_x \neq 0$), the frequency of the edge modes moves away from zero at $q_x \neq 0$ as shown in Fig. 3. Finally, in contrast to the deformed kagome lattice [28] where the SSS and ZMs are localized on opposite domain walls, in our systems the ZMs and SSS are on the same domain wall. Typically, ZMs and SSS cannot be localized on the same domain wall, because they will be lifted to finite frequency in the presence of hybridization between them. In our system, such hybridization is prohibited by the mirror symmetry, because for each domain, its ZMs and SSS have opposite mirror parity (even versus odd).

To conclude this section, we would like to point out that this topological index and zero modes can also be characterized by a low-energy continuum theory (SM [37] Sec. SM5) using a Dirac Hamiltonian and the Jackiw-Rebbi analysis [38,39].

Mirror-protected corner states. Mirror symmetric systems in the BDI class where the mirror reflection operator commutes TRS and chiral symmetry operators can have mirror symmetry protected zero-frequency corner modes [10,40]. To look for such corner states, we create a diamond-shaped island of one phase inside another rhombus-shaped phase with periodic boundary conditions for the rhombus in both directions (Fig. 4). The top and the bottom corners of the diamond are invariant under a vertical mirror passing through them. In Figs. 4(a) and 4(b), we see that when the inner island phase is $\delta = -13/42$ and the outer phase is $\delta = 1/3$, there are zero-frequency corner modes localized at the top and the bottom corners, the top (bottom) one being odd (even) under the vertical mirror reflection. The situation is more curious when the inner island is $\delta = 1/3$ and the outer phase is $\delta = -13/42$ [Figs. 4(c) and 4(d)]. There are still two zero-frequency corner modes, one of the odd and the other even under the vertical mirror reflection, but they are both localized at the right and left corners.

The topological nature and the origin of these corner modes can be easily understood using the standard approach of HOTS (SM [37] Sec. SM6). When the domain wall between the two phases is tilted such that the domain wall is not invariant under reflection, the localized states at the domain wall become massive, meaning that the spectrum is gapped at $\omega = 0$. Moreover, two oppositely tilted domain walls have opposite sign of the mass m; the sign of the mass m depends on the sign of the angle of tilt of the domain wall. Therefore, at the corner both δ (across the domain boundary) and m (along the domain boundary) change sign. As is elaborated in the SM [37] Sec. SM6, depending on the sign of the mass m, the amplitude of the zero-frequency mode ($\sim e^{-mx}$) may either decrease or increase as we move away from the corner point ($x = 0$). If the amplitude increases exponentially as we move away from this corner, it implies that this zero mode is localized at the next corner along the direction of the increasing amplitude. This theory analysis is in perfect agreement with numerical simulations. Furthermore, these corner modes persist even when the corner is not mirror invariant, as long as the bulk structures have mirror symmetry (see SM [37] Sec. SM7), which implies that this HOTS is "intrinsic" [10,40].

Conclusions. In this Letter we demonstrated how spatial symmetries can protect the higher-order topological phase in Maxwell frames and give rise to zero-frequency topological edge and corner modes. Furthermore, these edge and corner modes are pinned to zero frequency due to the inherent chiral symmetry of Maxwell frames pointed out in Ref. [28]. This chiral symmetry is often used as an approximate symmetry in fermionic systems (except in the case of superconductors), but in the case of Maxwell lattices it is exact. As mentioned earlier, our system falls under the BDI class of Altland-Zirnbauer classification; it has been known in the literature [10,40] that mirror symmetry that commutes with time reversal and chiral symmetry can protect corner modes in two dimensions in this

class. Our structure is an example of this in classical systems. This system should be straightforwardly experimentally realized using hard plastic parts and hinges similar to what was done in Ref. [41] for a deformed kagome lattice, with the three extra point masses [red points 4–6 in Fig. 1(a)] in our system needing to be put on fixed rails such that they can only move along the corresponding rails.

Acknowledgments. S.S. thanks Xiaohan Wan for many discussions on this topic. This work was supported in part by the Office of Naval Research MURI N00014-20-1-2479.

[1] M. Z. Hasan and C. L. Kane, Rev. Mod. Phys. **82**, 3045 (2010).
[2] X.-L. Qi and S.-C. Zhang, Rev. Mod. Phys. **83**, 1057 (2011).
[3] K. V. Klitzing, G. Dorda, and M. Pepper, Phys. Rev. Lett. **45**, 494 (1980).
[4] C.-X. Liu, S.-C. Zhang, and X.-L. Qi, Annu. Rev. Condens. Matter Phys. **7**, 301 (2016).
[5] C. L. Kane and E. J. Mele, Phys. Rev. Lett. **95**, 146802 (2005).
[6] B. A. Bernevig, T. L. Hughes, and S.-C. Zhang, Science **314**, 1757 (2006).
[7] W. A. Benalcazar, B. A. Bernevig, and T. L. Hughes, Science **357**, 61 (2017).
[8] W. A. Benalcazar, B. A. Bernevig, and T. L. Hughes, Phys. Rev. B **96**, 245115 (2017).
[9] F. Schindler, A. M. Cook, M. G. Vergniory, Z. Wang, S. S. Parkin, B. A. Bernevig, and T. Neupert, Sci. Adv. **4**, eaat0346 (2018).
[10] J. Langbehn, Y. Peng, L. Trifunovic, F. von Oppen, and P. W. Brouwer, Phys. Rev. Lett. **119**, 246401 (2017).
[11] E. Khalaf, Phys. Rev. B **97**, 205136 (2018).
[12] Z. Song, Z. Fang, and C. Fang, Phys. Rev. Lett. **119**, 246402 (2017).
[13] G. van Miert and C. Ortix, Phys. Rev. B **98**, 081110(R) (2018).
[14] B. Xie, H.-X. Wang, X. Zhang, P. Zhan, J.-H. Jiang, M. Lu, and Y. Chen, Nat. Rev. Phys. **3**, 520 (2021).
[15] H. Fan, B. Xia, L. Tong, S. Zheng, and D. Yu, Phys. Rev. Lett. **122**, 204301 (2019).
[16] H. Wakao, T. Yoshida, H. Araki, T. Mizoguchi, and Y. Hatsugai, Phys. Rev. B **101**, 094107 (2020).
[17] M. Serra-Garcia, V. Peri, R. Süsstrunk, O. R. Bilal, T. Larsen, L. G. Villanueva, and S. D. Huber, Nature (London) **555**, 342 (2018).
[18] J. Attig, K. Roychowdhury, M. J. Lawler, and S. Trebst, Phys. Rev. Res. **1**, 032047(R) (2019).
[19] H. Xue, Y. Yang, F. Gao, Y. Chong, and B. Zhang, Nat. Mater. **18**, 108 (2019).
[20] X. Ni, M. Weiner, A. Alu, and A. B. Khanikaev, Nat. Mater. **18**, 113 (2019).
[21] M. Proctor, P. A. Huidobro, B. Bradlyn, M. B. de Paz, M. G. Vergniory, D. Bercioux, and A. García-Etxarri, Phys. Rev. Res. **2**, 042038(R) (2020).
[22] G. van Miert and C. Ortix, npj Quantum Mater. **5**, 63 (2020).
[23] M. A. J. Herrera, S. N. Kempkes, M. B. de Paz, A. García-Etxarri, I. Swart, C. M. Smith, and D. Bercioux, Phys. Rev. B **105**, 085411 (2022).
[24] A. Saremi and Z. Rocklin, Phys. Rev. B **98**, 180102(R) (2018).
[25] E. Khalaf, W. A. Benalcazar, T. L. Hughes, and R. Queiroz, Phys. Rev. Res. **3**, 013239 (2021).
[26] J. C. Maxwell, London, Edinburgh Dublin Philos. Mag. J. Sci **27**, 294 (1864).
[27] T. Lubensky, C. Kane, X. Mao, A. Souslov, and K. Sun, Rep. Prog. Phys. **78**, 073901 (2015).
[28] C. L. Kane and T. C. Lubensky, Nat. Phys. **10**, 39 (2014).
[29] T. Neupert and F. Schindler, in *Topological Matter: Lectures from the Topological Matter School 2017* (Springer, Berlin, 2018), pp. 31–61.
[30] Y. Ren, Z. Qiao, and Q. Niu, Phys. Rev. Lett. **124**, 166804 (2020).
[31] S. Imhof, C. Berger, F. Bayer, J. Brehm, L. W. Molenkamp, T. Kiessling, F. Schindler, C. H. Lee, M. Greiter, T. Neupert *et al.*, Nat. Phys. **14**, 925 (2018).
[32] C. R. Calladine, Int. J. Solids Struct. **14**, 161 (1978).
[33] A. Altland and M. R. Zirnbauer, Phys. Rev. B **55**, 1142 (1997).
[34] A. Kitaev, in *Advances in Theoretical Physics: Landau Memorial Conference*, edited by V. Lebedev and M. Feigel'man, AIP Conf. Proc. No. 1134 (American Institute of Physics, Melville, NY, 2009), pp. 22–30.
[35] S. Ryu, A. P. Schnyder, A. Furusaki, and A. W. Ludwig, New J. Phys. **12**, 065010 (2010).
[36] C.-K. Chiu, J. C. Y. Teo, A. P. Schnyder, and S. Ryu, Rev. Mod. Phys. **88**, 035005 (2016).
[37] See Supplemental Material at http://link.aps.org/supplemental/10.1103/PhysRevB.108.L060103 for details of the compatibility matrix, its decomposition along the mirror invariant line in the Brillouin zone, the derivation of the low energy theory, Jackiw-Rebbi analysis for the domain wall and corner zero modes, etc.
[38] R. Jackiw and C. Rebbi, Phys. Rev. D **13**, 3398 (1976).
[39] B. A. Bernevig, *Topological Insulators and Topological Superconductors* (Princeton University Press, Princeton, NJ, 2013).
[40] M. Geier, L. Trifunovic, M. Hoskam, and P. W. Brouwer, Phys. Rev. B **97**, 205135 (2018).
[41] D. Z. Rocklin, S. Zhou, K. Sun, and X. Mao, Nat. Commun. **8**, 14201 (2017).